



Universiteit
Leiden
The Netherlands

Simulation of the cosmic ray impact on the TES detectors of SPICA/SAFARI

Stockmans, T.A.; Almasi, A.; Stever, S.L.; Khosropanah, P.

Citation

Stockmans, T. A., Almasi, A., Stever, S. L., & Khosropanah, P. (2022). Simulation of the cosmic ray impact on the TES detectors of SPICA/SAFARI. *Journal Of Low Temperature Physics*, 209, 482-492. doi:10.1007/s10909-022-02815-8

Version: Publisher's Version
License: [Creative Commons CC BY 4.0 license](https://creativecommons.org/licenses/by/4.0/)
Downloaded from: <https://hdl.handle.net/1887/3561375>

Note: To cite this publication please use the final published version (if applicable).



Simulation of the Cosmic Ray Impact on the TES Detectors of SPICA/SAFARI

T. A. Stockmans¹ · A. Almasi² · S. L. Stever^{3,4} · P. Khosropanah²

Received: 2 November 2021 / Accepted: 29 June 2022 / Published online: 5 September 2022
© The Author(s) 2022

Abstract

The data from the Planck and Herschel space observatories revealed that the cosmic rays at L2 orbit can have a significant impact on the performance of scientific instruments. In this paper, we present our simulation results of such impacts on SAFARI/SPICA, a far-infrared spectrometer equipped with transition-edge sensors (TESs). These TESs are fabricated on SiN membranes and suspended by long and thin SiN legs that thermally isolate them from the surrounding silicon structure (wafer). Cosmic rays that pass through this surrounding structure deposit a portion of their energy, leading to temperature fluctuations in the wafer. These temperature fluctuations are sensed by the TES detectors as an effective bath temperature and result in additional noise. To simulate the impact, we generate a 2D model of the wafer and the suspended TESs in COMSOL 5.4. This 2D model is bombarded with 128 randomly generated cosmic rays according to the observed energy distributions at L2. Subsequently, the temperature fluctuations at different points on the wafer are estimated. Our results show that these thermal fluctuations, as well as the calculated additional TES noise caused by them, depend strongly on the heat-sink design of the wafer. We study the impact of the different heat sink designs on the noise profile of the system. Later, these results are compared to the SAFARI instrument noise requirements.

Keywords TES · Cosmic rays · SPICA · SAFARI · Heat transfer

✉ T. A. Stockmans
stockmans@strw.leidenuniv.nl

¹ Leiden Observatory, Leiden University, Niels Bohrweg 2, 2333 CA Leiden, The Netherlands

² Netherlands Institute for Space Research (SRON), Niels Bohrweg 4, 2333 CA Leiden, The Netherlands

³ Kavli IPMU (WPI), UTIAS, The University of Tokyo, Kashiwa, Chiba 277-8583, Japan

⁴ Okayama University, Tsushimanaka 3-1-1 Kita-ku, Okayama City, Okayama 700-8530, Japan

1 Introduction

The SPICA telescope was a joint collaboration between the European and Japanese space organizations ESA and JAXA. The mission was designed as the newest space mission observing in the mid- and far-infrared, as a successor to the highly successful Herschel mission [1].

The satellite design supported a 2.5 m mirror, actively cooled to below 8 Kelvin in order to reduce the thermal radiation of the mirror itself. The three instruments on board operated in the mid- and far-infrared: SAFARI, SMI, and POL [1]. SPICA's powerful detectors provide two orders of magnitude greater sensitivity compared to the previous-generation Herschel and SOFIA instruments, in part because the SPICA instruments are not limited by radiation coming from the telescope itself. This increased sensitivity would have enabled the SAFARI, POL, and SMI instruments to investigate the spectroscopic details of both close-by and far away galaxies in unprecedented detail [2–6].

For the SAFARI instrument, there are four focal plane arrays (FPAs). To reach the mission requirements of extremely low noise, field of view, and Nyquist sampling of the spectra, each of these FPAs should hold around 4000 low noise TESs [7]. These TESs are made from Ti/Au patterned on an island of SiN, next to an absorber made of tantalum (Ta). This island is suspended to a Si wafer structure using four long SiN legs [8]. Above these islands are pyramidically shaped horns which focus the light on the TES and absorber. All important dimensions are also listed in [8].

Cosmic rays (CRs) originate either from the sun or at high energetic events outside of our solar system. The CRs at L2 orbit consist of 89% protons, as found by the Planck satellite [9]. The impact rate for all CRs at L2 as reported by [10] for the Herschel telescope is between 2.8 and 3.5 counts/s cm², comparable to the rate found by Planck [9]. The energy distribution of these CRs extends over a large domain as can be seen in [11]. The SPICA design includes a cosmic radiation shield for protons less energetic than 35 MeV. Hence, we have a clear cut-off below the 35 MeV energy level.

This paper focuses on the introduced noise from the thermal heating of the wafer due to CR impact. When a CR hits either the supporting wafer or the suspending legs of the structure, it induces a thermal spike. The photon-induced power depends on the bath temperature T_{bath} . This bath temperature is the temperature of the suspending legs. Therefore, when these legs suffer from thermal spikes, there will be additional noise on the readout of the TESs.

2 Methods

The heat transfer simulation is conducted using COMSOL. The simulations shown in this work are conceptually close to earlier work by Marcel Bruin for SAFARI and a similar simulation for the X-IFU detector on Athena by [12].

The geometry was defined using the latest design provided by the SAFARI engineering team. The wafer is a perforated piece of pure silicon with outer

dimensions of $31 \times 24 \times 0.35 \text{ mm}^3$. The holes are in the z -direction, in the centre of which the TESs are suspended. Because of the symmetry and relative small size in the z -direction and computational restrictions, we use a 2D (x, y) model of the wafer.

At the beginning of the simulations, the whole wafer is initialized at a temperature of 50mK. During the simulations, 26.7 CRs hit the wafer on average every second. This impact rate is calculated using the dimensions of the wafer and the rate of impact as given by [11].

The energy of the impacting CRs is randomly chosen from the energy distribution in [11]. To check whether the samples are a good representation of the distribution, we split the group of samples in half and calculated the total variation distance between both halves. When this total variation distance shrank below 0.05, both halves were similar enough to assume they were not dominated by outliers. The same assumption could subsequently be made for the group of samples as a whole, and we could treat the group of samples as a valid representation of the distribution as a whole. In this paper, we have a group of 128 samples that satisfy this condition. Each of these CRs has a random impact location and time assigned. The energy that each of these CRs would transfer to wafer after impact is calculated using the Bethe equation and considered as a heat event in the simulation.

Each CR is approximated as a circular heat source of $r = 10^{-4} \text{ m}$ with an exponential time behaviour [13]. With the two time constants controlling the exponential rise and fall time: $t_f = 10^{-10} \text{ s}$ and $t_r = 10^{-10.5} \text{ s}$, respectively.

In the simulation, the time sampling is nonlinear around each pulse. The time stepping is chosen in order to minimize the total amount of steps, while still being able to resolve at least 99.99% of the energy pulse using trigonometric integration. This time stepping only controls the points for which the temperature data is extracted. For the internal calculation of these temperature profiles, the simulation model is free to determine smaller step sizes in order to converge with numerical errors within the imposed tolerances.

A connection to a heat sink can influence the calculation by extracting heat from the wafer and actively cooling the structure. The simulation is run both without any heat sink connection and with four heat sink connections of varying efficiency. The connection to the heatsink is simulated as an extra thin strip of silicon added at the boundary of the wafer. The arbitrary size of this strip influences the total heat capacity of the wafer but is small enough not to affect the cooling capacities for the same total thermal conductance. The difference in heat conductivity of the cooling connection is the main influence on the efficiency of the cooling capacities. Four final heat sink connections are simulated with the properties as shown in Table 1.

The TESs are influenced by thermal changes in the wafer because their base power is a function of the thermal bath. The TESs are biased at a fixed voltage and have a rest current flowing through them, combining into a base power. This base power is a function of both the temperature of the TES and the temperature of the bath around it. This T_{bath} is the temperature of the wafer at the point of connection. The change in temperature on the wafer happens irregularly, so it presents itself as

Table 1 Properties of the connection to the heat sink in separate simulations

Set-up	G (W/K)	Width (mm)	Heat capacity (J/K)
1	2×10^{-7}	0.1	2.26×10^{-14}
2	2×10^{-6}	0.1	2.26×10^{-14}
3	2×10^{-8}	0.1	2.26×10^{-14}
4	2×10^{-8}	1	2.26×10^{-13}

Either the heat conduction rate (G) or the width is varied in every instance, the heat capacity of the heat sink connection is only dependent of the width

another noise source for the TESs. The base power follows the following equation [14]:

$$P_b = k(T_{\text{TES}}^n - T_{\text{bath}}^n) \quad (1)$$

where n is the thermal conductance exponent and k a constant depending on the thermal conductance, n and the TES temperature. Typical numbers are given in Table 2. If the change in base power is equally discretized in time, it can be transformed using the discrete Fourier transform to the Noise Equivalent Power (NEP) with the equation below. The data from the simulations is nonlinear, with more temporal sampling around the start of each impact. Therefore, the equal sampling in the time domain is done using a numerical interpolation.

$$\text{NEP} = \frac{P(f)}{\sqrt{\Delta f}} \quad (2)$$

The measurements are done with a frequency of around 100Hz as in [8]; so we highlight the NEP at this frequency in order to compare it with the other noise sources.

3 Results

To see the thermal increase due to the impact of CRs across the wafer, four different points on the wafer are probed. P1 is the central point, which is furthest from the cooling band. P2 and P3 lay at the extends of the legs on which the left

Table 2 Typical values for a dark TES [8]

Parameter	Value
P_b	20 fW
V_b	10 nV
T_{TES}	100 mK
n	3
k	$2.29 \times 10^{-11} \text{ W K}^n$

outermost TES are suspended. The last point, P4, is chosen to lay exactly at the point of impact of an CR. These points are visualized in Fig. 1.

When the connection to the heat sink is not simulated, the whole structure steadily heats up in time. The increase in temperature was analytically calculated, and verified by the simulation, to be 0.001K per 0.1MeV added energy from the CRs.

In Fig. 2, the thermal response of the different simulations is shown at the different points on the wafer. The spikes due to the near impacts show the same profile as the one without a heat sink. This outcome is expected because the initial cooling of these spikes is due to the spreading over the total wafer. It is interesting to note that, with the thermal external connection, the wafer is able to lose the extra energy resulting from each CR impact. For each of the simulated heat sink connections, the cooling rate is faster than the impact rate of the CRs and the wafer returns to 50 mK after each impact.

The thermal profiles are more dependent on the distance from the different CR impacts than to the efficiency of the thermal connection. The amplitude of the spikes, however, differs between the different heat sink connections. The effects on the amplitudes are most visible for P2 and P3. The closer a CR is to the heat sink, the sooner the cooling process starts. The CRs that induce the clearest heat surges at a measurement point are the CRs closest to the measurement point. Since point P2 and P3 lie close to the cooling boundary, the most significant CR impacts are also closer to the cooling boundary and more damped by the cooling connection. P1 is least affected by the fast dampening because it is at the centre of the wafer and thus relatively far from the boundary. On the other hand, P4 does not show this effect since it is completely dominated by the CR hit at its location, and the peak amplitude of that CR hit is only a function of its energy.

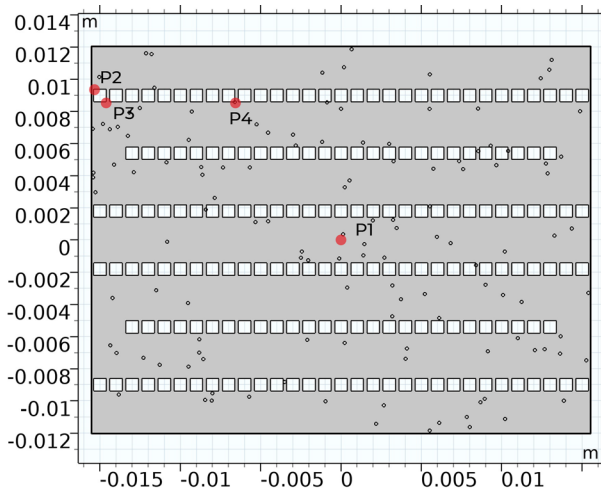


Fig. 1 Points at which the thermal behaviour is measured in the simulations (P1–P4) are overlaid on the geometry in red. The small black circles are the locations where the CR impact the wafer. The numbers on the axes are the distance in meters from the centre of the wafer (Color figure online)

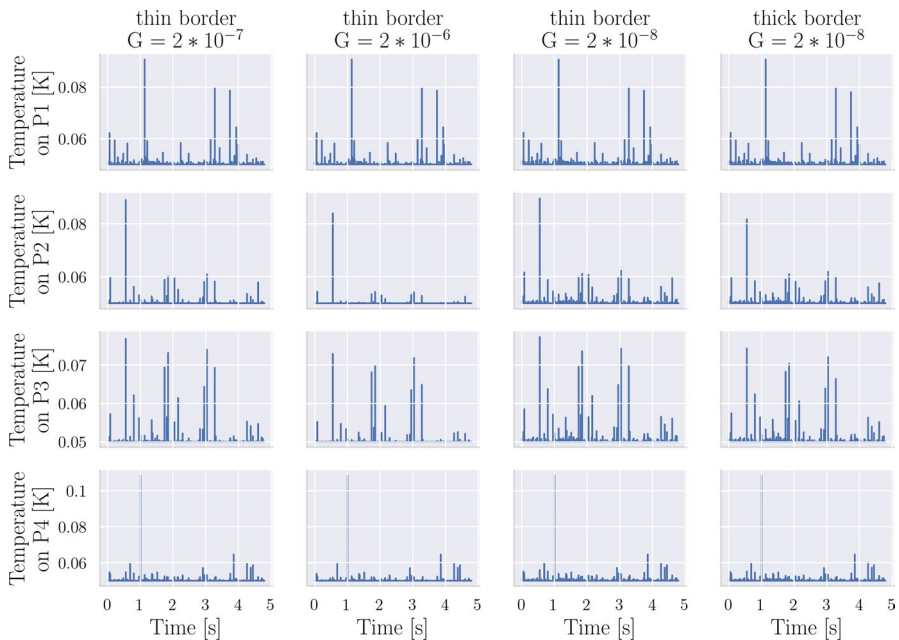


Fig. 2 The temperature variation in time for the different measurement points (P1–P4) on the rows and with the different thermal connections on the columns. The distribution of the peaks is mostly a function of the location of the measurement, while the total height of these peaks is determined mostly by the thermal connection (Color figure online)

In Fig. 3, the cooling of a single CR impact is shown as dominated by the cooling efficiency. The difference in cooling rate becomes apparent both in peak amplitude and the cooling timescale. We define the cooling timescale as the time the wafer takes to reach the peak temperature and cool again to $\frac{1}{e}$ times of the peak amplitude. Below we give the linear estimations of this quantity for all configurations.

The most efficient thermal connection displays the fastest cooling timescale (0.13 ms) and lowest peak amplitude (50.05 mK). The cooling timescale (0.26 ms) and peak amplitude (50.48 mK) of the medium heat sink follows. This succession is inline with our expectations.

Also, note that the thick and thin heat sink connections (resp. set-up 4 and 3) compare very well in both peak amplitude (respectively 51.23 mK, 51.4 mK) and time scale (respectively 1.2 ms, 1.1 ms). So we can conclude that the used set-up does not heavily depend on the arbitrarily chosen geometry of the heat sink connection, but rather on the thermal conductance of the heat sink.

Without a heat sink, the outcome is different. The structure cannot stabilize back to 50 mK after each CR impact. Therefore, the induced NEP at 100 Hz is on the order of $10^{-17} \text{ W}/\sqrt{\text{Hz}}$, which is two orders of magnitude higher than the noise requirement for SAFARI.

In Fig. 4, the NEP of each point is plotted. The NEP requirement of 2×10^{-19} is marked as well as the 100 Hz line. When the NEP is below this NEP level, the noise requirements of SAFARI can be met. We make use of multiple temporal

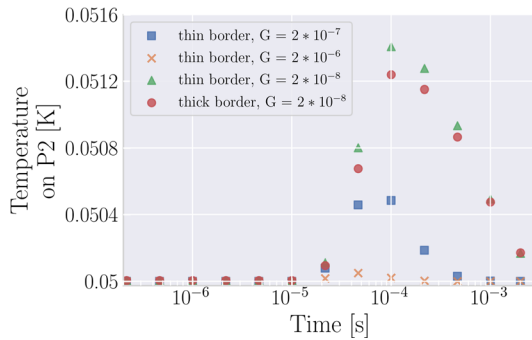


Fig. 3 Close-up of the cooling time profile of the CR impact at 3.742s as viewed from P2. This CR impact is the most central isolated impact. The cooling decay as viewed at P2 can be assumed to be dominated by the heat sink connection instead of thermal dissipation. The different thermal connections are displayed with different colours and markers. The time is shown logarithmically, starting from 10^{-5} s when the temperature increase has spread to P2, until 3×10^{-3} s when the peak is subsided in the two most efficient cases (Color figure online)

interpolation resolutions to make sure that we are not limited by undersampling of the results of our simulations. The difference between different temporal interpolation resolutions is most evident in the second set-up. This difference is most likely due to the fact that the temperature increases are smallest for this set-up, so small numerical differences between interpolations with different resolutions will have a bigger impact on the calculation of the NEP.

Table 3 shows the weighted average of the NEP at 100Hz at each point for each heat sink connection. Including a connection to the heat sink has an important effect on the total noise levels on the detector, which drops by at least an order of magnitude. The thermal connection with a $G = 2 \times 10^{-6}$ is the set-up with the lowest noise levels, as could be expected. For this set-up, the noise is well below the requirement noise level for all points on the wafer. Finally, the thermal connection with $G = 2 \times 10^{-8}$ does not cool efficiently enough and lies significantly above the noise requirement level for all measurement points.

4 Discussion

In this work, a cooling connection is implemented with an additional band of silicon around the wafer. Although the dimensions of this band do not show a significant effect on our results, this band is still a basic approximation of the actual thermal connection. Instead, wire bonds could be approximated with a golden band of comparable dimensions.

The design of the cooling connection is constrained by multiple factors such as cost and limited space, so there is a limited number of wire bonds available as well as a limited area to which they can be connected. Furthermore, more effects become important with a transfer of temperature between two metals, such as Kapitza coupling [12]. Follow-up research should take all these constraints and extra physics

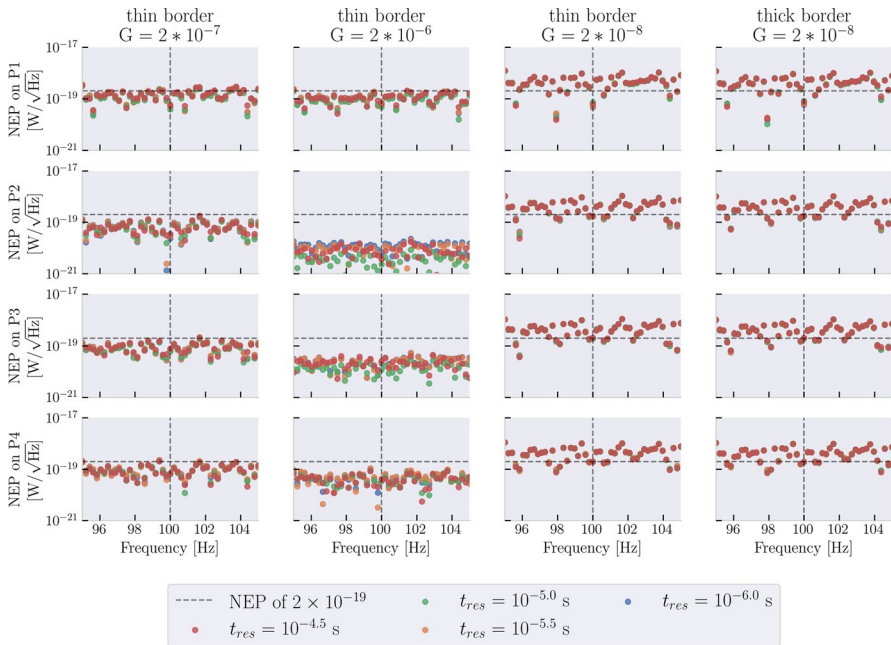


Fig. 4 The noise equivalent power (NEP) as a function of frequency. Each row displays a different heat sink connection and each column a different measuring location (P1–P4). The different colours depict different interpolation step sizes. This calculation is conducted as if there is a unique TES connected to each of these points (Color figure online)

Table 3 The weighted average NEP level at 100Hz for the different points and simulations

	Set-up 1	Set-up 2	Set-up 3	Set-up 4
P1	$1.4 \pm 0.6 \times 10^{-19}$	$1.0 \pm 0.4 \times 10^{-19}$	$5 \pm 2 \times 10^{-19}$	$4 \pm 2 \times 10^{-19}$
P2	$0.7 \pm 0.3 \times 10^{-19}$	$0.6 \pm 0.3 \times 10^{-20}$	$4 \pm 2 \times 10^{-19}$	$4 \pm 2 \times 10^{-19}$
P3	$0.9 \pm 0.4 \times 10^{-19}$	$1.9 \pm 0.9 \times 10^{-20}$	$4 \pm 2 \times 10^{-19}$	$4 \pm 2 \times 10^{-19}$
P4	$0.9 \pm 0.4 \times 10^{-19}$	$4.3 \pm 2 \times 10^{-20}$	$4 \pm 2 \times 10^{-19}$	$4 \pm 2 \times 10^{-19}$

This value was calculated by taking the average NEP between 95 and 105 Hz for each resolution and take the weighted average of those in turn. All values are in W/\sqrt{Hz}

into account to give a more accurate estimation of the requirements of the thermal heat sink.

Another important issue is the connection between the wafer and other structures. The wafer is mounted on a larger structure with the read-out electronics, the LC-circuits, and an aluminium support structure. The mounting of the wafer to these structures is done using four golden clamps on the sides. It means that the induced heat from the CRs will be distributed over a larger structure, with a higher heat capacity. On the flip side, CR hits on these other parts will also reach the wafer. The complexity of these simulations desires more work. The work of [12] shows some of

the additional upgrades to CR impact simulations in good detail, especially cooling through the golden wire bonding and the layer structure.

The final main caveat is the singular focus on the primary CRs and the neglecting of other particles. When a high-energy proton goes through the shielding, it will knock out some electrons as well. Using the simulation program GEANT4 designed for particle cascade simulations, [11] found that the secondary particles contribute about $1.3 \text{ counts/s/cm}^2$ extra on the detector. However, the used impact rate by [11] is already around 1 counts/s/cm^2 higher than found by Herschel and Planck. Therefore, the deviations caused by secondary particles are not expected to be high.

There are multiple other ways in which CRs might influence the detection and noise limits. Including direct hits on the TESs, hits on the suspending legs of the TES or hits on the LC-circuits connected to each TES. Each of these scenarios is beyond the scope of this study, but are important in creating an overview of all the complications with which CRs might influence the instrument in L2 orbit.

5 Conclusion

The goal for SAFARI is to have a sensitivity characterized by an NEP of $2 \times 10^{-19} \text{ W}/\sqrt{\text{Hz}}$. This high sensitivity is due to the TES detectors and the cooled mirror of SPICA itself. The noise levels for these TES detectors can be seriously dominated by cosmic rays as was seen previously at Planck and Herschel.

Using the simulation program COMSOL 5.4, we have created a 2D model of the structure on which the TESs are suspended. This structure was bombarded with 128 randomly generated cosmic rays following observed property distributions at L2. When no connection to the heat sink is implemented, the NEP effect due to this bombardment is shown to be $10^{-17} \text{ W}/\sqrt{\text{Hz}}$.

Additionally, 4 different connections to the heat sink are simulated. The cooling in each simulation is mainly influenced by the thermal conductance, which determined its efficiency and cooling time scale. When the thermal conductance is $2 \times 10^{-7} \text{ W/K}$, the cooling was sufficient to keep the noise lower than the operating requirement for SAFARI on the whole wafer. With a 10 times less efficient cooling, the whole wafer experiences noise levels exceeding this requirement.

With this study, we show that the thermal noise due to CRs has a serious impact on the noise budget of SAFARI instrument. However, more research is desired as a follow-up study in three main areas:

1. A detailed study of the thermal connection to the heat sink and other thermally connected elements.
2. The precise energy distribution and impact rate of the CR after interaction with the shielding of the telescope.
3. A verification of the thermal simulations using proton and α -particle sources.

These studies will show the feasibility of the desired sensitivity for SAFARI and comparable instruments in the future.

Acknowledgements The authors would like to express their thanks to the members of the SAFARI engineering team, specifically Marcel Bruin and Saad Ilyas, for the useful discussions and details of the instrument layout.

Declarations

Conflict of interest The authors declare that they have no conflict of interest.

Open Access This article is licensed under a Creative Commons Attribution 4.0 International License, which permits use, sharing, adaptation, distribution and reproduction in any medium or format, as long as you give appropriate credit to the original author(s) and the source, provide a link to the Creative Commons licence, and indicate if changes were made. The images or other third party material in this article are included in the article's Creative Commons licence, unless indicated otherwise in a credit line to the material. If material is not included in the article's Creative Commons licence and your intended use is not permitted by statutory regulation or exceeds the permitted use, you will need to obtain permission directly from the copyright holder. To view a copy of this licence, visit <http://creativecommons.org/licenses/by/4.0/>.

References

1. P.R. Roelfsema, H. Shibai, L. Armus, D. Arrazola, M. Audard, M.D. Audley, C.M. Bradford, I. Charles, P. Dieleman, Y. Doi, L. Duband, M. Eggens, J. Evers, I. Funaki, J.R. Gao, M. Giard, A. Di Giorgio, L.M. Fernández, M. Griffin, F.P. Helmich, R. Hijmering, R. Huisman, D. Ishihara, N. Isobe, B. Jackson, H. Jacobs, W. Jellema, I. Kamp, H. Kaneda, M. Kawada, F. Kemper, F. Kerschbaum, P. Khosropanah, K. Kohno, P.P. Kooijman, O. Krause, J. Van Der Kuur, J. Kwon, W.M. Laauwen, G. De Lange, B. Larsson, D. Van Loon, S.C. Madden, H. Matsuhara, F. Najarro, T. Nakagawa, D. Naylor, H. Ogawa, T. Onaka, S. Oyabu, A. Poglitsch, V. Reveret, L. Rodriguez, L. Spinoglio, I. Sakon, Y. Sato, K. Shinozaki, R. Shipman, H. Sugita, T. Suzuki, F.F. Van Der Tak, J.T. Redondo, T. Wada, S.Y. Wang, C.K. Wafelbakker, H. Van Weers, S. Withington, B. Vandenbussche, T. Yamada, I. Yamamura, *Publ. Astron. Soc. Austral.* **35**, 2018 (2018). <https://doi.org/10.1017/pasa.2018.15>
2. E. Egami, S. Gallerani, R. Schneider, A. Pallottini, L. Vallini, E. Sobacchi, A. Ferrara, S. Bianchi, M. Bocchio, S. Marassi, L. Armus, L. Spinoglio, A.W. Blain, M. Bradford, D.L. Clements, H. Dannerbauer, J.A. Fernández-Ontiveros, E. González-Alfonso, M.J. Griffin, C. Gruppioni, H. Kaneda, K. Kohno, S.C. Madden, H. Matsuhara, F. Najarro, T. Nakagawa, S. Oliver, K. Omukai, T. Onaka, C. Pearson, I. Perez-Fournon, P.G. Pérez-González, D. Schaerer, D. Scott, S. Serjeant, J.D. Smith, F.F. Van Der Tak, T. Wada, H. Yajima, *Publ. Astron. Soc. Austral.* **35**(2018), 1 (2018). <https://doi.org/10.1017/pasa.2018.41>
3. L. Spinoglio, A. Alonso-Herrero, L. Armus, M. Baes, J. Bernard-Salas, S. Bianchi, M. Bocchio, A. Bolatto, C. Bradford, J. Braine, F.J. Carrera, L. Ciesla, D.L. Clements, H. Dannerbauer, Y. Doi, A. Efstathiou, E. Egami, J.A. Fernández-Ontiveros, A. Ferrara, J. Fischer, A. Franceschini, S. Gallerani, M. Giard, E. González-Alfonso, C. Gruppioni, P. Guillard, E. Hatziminaoglou, M. Imanishi, D. Ishihara, N. Isobe, H. Kaneda, M. Kawada, K. Kohno, J. Kwon, S. Madden, M.A. Malkan, S. Marassi, H. Matsuhara, M. Matsuura, G. Miniutti, K. Nagamine, T. Nagao, F. Najarro, T. Nakagawa, T. Onaka, S. Oyabu, A. Pallottini, L. Piro, F. Pozzi, G. Rodighiero, P. Roelfsema, I. Sakon, P. Santini, D. Schaerer, R. Schneider, D. Scott, S. Serjeant, H. Shibai, J.D. Smith, E. Sobacchi, E. Sturm, T. Suzuki, L. Vallini, F. Van der Tak, C. Vignali, T. Yamada, T. Wada, L. Wang, *Publ. Astron. Soc. Austral.* **34**, 2017 (2017). <https://doi.org/10.1017/pasa.2017.48>
4. C. Gruppioni, L. Ciesla, E. Hatziminaoglou, F. Pozzi, G. Rodighiero, P. Santini, L. Armus, M. Baes, J. Braine, V. Charmandaris, D.L. Clements, N. Christopher, H. Dannerbauer, A. Efstathiou, E. Egami, J.A. Fernández-Ontiveros, F. Fontanot, A. Franceschini, E. González-Alfonso, M. Griffin, H. Kaneda, L. Marchetti, P. Monaco, T. Nakagawa, T. Onaka, A. Papadopoulos, C. Pearson, I. Pérez-Fournon, P. Pérez-González, P. Roelfsema, D. Scott, S. Serjeant, L. Spinoglio, M. Vaccari, F. van der Tak, C. Vignali, L. Wang, T. Wada, *Publ. Astron. Soc. Austral.* **34**, 2017 (2017). <https://doi.org/10.1017/pasa.2017.49>

5. E. González-Alfonso, L. Armus, F.J. Carrera, V. Charmandaris, A. Efstathiou, E. Egami, J.A. Fernández-Ontiveros, J. Fischer, G.L. Granato, C. Gruppioni, E. Hatziminaoglou, M. Imanishi, N. Isobe, H. Kaneda, D. Koziel-Wierzbowska, M.A. Malkan, J. Martín-Pintado, S. Mateos, H. Matsuhara, G. Miniutti, T. Nakagawa, F. Pozzi, F. Rico-Villas, G. Rodighiero, P. Roelfsema, L. Spinoglio, H.W. Spoon, E. Sturm, F. van der Tak, C. Vignali, L. Wang, *Publ. Astron. Soc. Austral.* **34**, 2017 (2017). <https://doi.org/10.1017/pasa.2017.46>
6. J.A. Fernández-Ontiveros, L. Armus, M. Baes, J. Bernard-Salas, A.D. Bolatto, J. Braine, L. Ciesla, I. De Looze, E. Egami, J. Fischer, M. Giard, E. González-Alfonso, G.L. Granato, C. Gruppioni, M. Imanishi, D. Ishihara, H. Kaneda, S. Madden, M. Malkan, H. Matsuhara, M. Matsuura, T. Nagao, F. Najarro, T. Nakagawa, T. Onaka, S. Oyabu, M. Pereira-Santaella, I. Pérez Fournon, P. Roelfsema, P. Santini, L. Silva, J.D. Smith, L. Spinoglio, F. van der Tak, T. Wada, R. Wu, *Publ. Astron. Soc. Austral.* **34**(2017) (2017). <https://doi.org/10.1017/pasa.2017.43>
7. B.D. Jackson, P.A. De Korte, J. Van Der Kuur, P.D. Mauskopf, J. Beyer, M.P. Bruijn, A. Cros, J.R. Gao, D. Griffin, R. Den Hartog, M. Kiviranta, G. De Lange, B.J. Van Leeuwen, C. MacCuli, L. Ravera, N. Trappe, H. Van Weers, S. Withington, *IEEE Trans. Terahertz Sci. Technol.* **2**(1), 12 (2012). <https://doi.org/10.1109/TTHZ.2011.2177705>
8. P. Khosropanah, T. Suzuki, M.L. Ridder, R.A. Hijmering, H. Akamatsu, L. Gottardi, J. van der Kuur, J.R. Gao, B.D. Jackson, Millimeter, Submillimeter, and Far-Infrared Detectors and Instrumentation for Astronomy VIII **9914**, 99140B (2016). <https://doi.org/10.1117/12.2233472>
9. A. Catalano, P. Ade, Y. Atik, A. Benoit, E. Bréele, J.J. Bock, P. Camus, M. Chabot, M. Charra, B.P. Crill, N. Coron, A. Coulais, F.X. Désert, L. Fauvet, Y. Giraud-Héraud, O. Guillaudin, W. Holmes, W.C. Jones, J.M. Lamarre, J. Macías-Pérez, M. Martínez, A. Miniussi, A. Monfardini, F. Pajot, G. Patanchon, A. Pelissier, M. Piat, J.L. Puget, C. Renault, C. Rosset, D. Santos, A. Sauvé, L.D. Spencer, R. Sudiwala, *Astron. Astrophys.* **569**, 1 (2014). <https://doi.org/10.1051/0004-6361/201423868>
10. B. Horeau, O. Boulade, A. Claret, H. Feuchtgruber, K. Okumura, P. Panuzzo, A. Papageorgiou, V. Reveret, L. Rodriguez, M. Sauvage, Proceedings of the European Conference on Radiation and its Effects on Components and Systems, RADECS pp. 541–548 (2011). <https://doi.org/10.1109/RADECS.2011.6131435>
11. S. Lotti, E. Perinati, L. Natalucci, L. Piro, T. Mineo, L. Colasanti, C. MacCuli, *Nuclear Instruments and Methods in Physics Research. Section A: Accelerators, Spectrometers, Detectors and Associated Equipment* **686**, 31 (2012). <https://doi.org/10.1016/j.nima.2012.05.055>
12. S.L. Stever, P. Peille, M.P. Bruijn, A. Roussafi, S. Lotti, C. Macculi, R.M.J. Janssen, R. den Hartog, *J. Low Temp. Phys.* **199**(1–2), 264 (2020)
13. S.L. Stever, Characterisation and modelling of the interaction between sub-Kelvin bolometric detectors and cosmic rays. Ph.D. thesis, Université Paris-Saclay (2019). 2019SACLS009
14. L. Gottardi, A. Kozorezov, H. Akamatsu, J. Van Der Kuur, M.P. Bruijn, R.H. Den Hartog, R. Hijmering, P. Khosropanah, C. Lambert, A.J. Van Der Linden, M.L. Ridder, T. Suzuki, J.R. Gao, *Appl. Phys. Lett.* **105**(16), 1 (2014)

Publisher's Note Springer Nature remains neutral with regard to jurisdictional claims in published maps and institutional affiliations.